PHYSICAL REVIEW B **105**, 214503 (2022)

# Structural phase transition and superconductivity of ytterbium under high pressure

Qingzhuo Duan,[1] Junyu Shen,[1] Xin Zhong,[2,*] Haiyan Lu,[3,†] and Cheng Lu[1,‡]
[1]*School of Mathematics and Physics, China University of Geosciences (Wuhan), Wuhan 430074, China*
[2]*Key Laboratory of Functional Materials Physics and Chemistry of the Ministry of Education, College of Physics, and National Demonstration Center for Experimental Physics Education, Jilin Normal University, Changchun 130103, China*
[3]*Science and Technology on Surface Physics and Chemistry Laboratory, P.O. Box 9-35, Jiangyou 621908, China*

(Received 23 January 2022; revised 19 May 2022; accepted 19 May 2022; published 3 June 2022)

Recent advances in theory and experiment declare the rare-earth (RE) hydrogen-rich compound $\mathrm{LaH}_{10}$ is a near room-temperature superconductor under high pressure. To understand the underlying mechanism of superconductivity and explore the crucial role of lanthanides in forming the RE-based polyhydrides, we here perform a theoretical study on the structural phase transition and superconductivity of late lanthanide ytterbium (Yb) metal under high pressure up to 240 GPa. Two alternative structures, $R\bar{3}m$ and $I4/mmm$ phases, of Yb are presented. Most interestingly, the $P6_3/mmc$ phase of Yb is serendipitously discovered to be a superior superconductor with a critical temperature value of 19.5 K at 160 GPa, which is higher than other known RE elemental superconductors. The present findings establish an alternative structural phase transition sequence of Yb, which offers insights for further understanding the vital physics mechanisms of a lanthanide-based superconductor.

DOI: 10.1103/PhysRevB.105.214503

## I. INTRODUCTION

The element hydrogen can form a metallic solid under high pressure with strong electron-phonon coupling (EPC) and high Debye temperature, which are crucial for understanding the microscopic mechanism of high-critical-temperature ($T_c$) superconductivity [1]. However, until now, to attain the metallization of hydrogen is still a challenge. Ashcroft [2] suggested that the “chemical precompression” of hydrogen would induce compressed hydrides to achieve the metallic state of hydrogen under much lower pressure. Many theoretical calculations and experimental syntheses confirm the reliability of this proposal. With the developments of supercomputers and high-pressure techniques, a great deal of hydrogen-rich superconductors have been discovered, such as hydrogen sulfides ($H_2S$ and $H_3S$ [3–5]), lanthanide polyhydrides ($\mathrm{LaH}_{10}$, $\mathrm{CeH}_{10}$, and $\mathrm{YbH}_{10}$ [6–9]), and graphenelike polyhydrides ($\mathrm{HfH}_{10}$ and $\mathrm{LuH}_{10}$ [10]), among which $\mathrm{LaH}_{10}$ has been predicted to be a superior superconductor with a $T_c$ value of 280 K at 210 GPa. Subsequent experiments verified that the hydrogen-rich $\mathrm{LaH}_{10}$ compound is indeed a near room-temperature superconductor under megabar pressure with a high-$T_c$ of 250 K [11]. The metallization and high superconductivity of the compressed $\mathrm{LaH}_{10}$ hydride are tightly related to the “chemical precompression” from La atoms. Similar rare-earth (RE)-based hydrogen-rich superconductors are also found under high pressure, such as $\mathrm{CeH}_{10}$ and $\mathrm{YbH}_{10}$. One key question, what is the exact role the RE atoms are playing in these hydrogen-rich superconductors? So far, the generally accepted conclusions are the following: (i) the RE atoms help in stabilizing the H clathrates at relatively lower pressure, (ii) the RE atoms contribute electrons to the H cages, and (iii) the $s$ states of H atoms mainly contribute at the Fermi level leading to the strong EPC and hence a high $T_c$. Similar results have been reported in the lanthanide polyhydride high-temperature superconductors [7]. We thus extend this study to explore the structural evolution and superconductivity of lanthanide metal Yb under high pressure, which may offer crucial insights for exploration of the structures and electronic properties as well as the underlying superconducting mechanisms of the RE-based hydrogen-rich superconductors.

More than 20 transition metals (TMs) have been found to be superconductors under ambient or high pressure, for instance, Nb ($T_c = 9.9\,\mathrm{K}$), Tc ($T_c = 8.2\,\mathrm{K}$), Ta ($T_c = 4.5\,\mathrm{K}$), and Fe ($T_c = 2.1\,\mathrm{K}$) [12,13]. A generally accepted conclusion is that the universal superconductivities of TMs are attributed to the $d$ orbitals of these TMs, which are capable of accommodating ten electrons and contribute significantly to the electronic density of states at the Fermi level ($N_{E_F}$) [12,14]. In fact, based on the Bardeen-Cooper-Schrieffer (BCS) theory [15–17], the EPC parameter $\lambda$ is equal to $N(E_F)\langle g^2\rangle/[M\langle\omega^2\rangle]$. It is not hard to speculate that the average electronic density of states of $d$ orbitals near the Fermi level ($N_{nE_F-d}$) is closely related to the EPC interactions. Similar to TMs, the 4$d$ orbitals of lanthanides also have the ability to hold ten electrons. These orbitals coupling with high-frequency phonons effectively resist the destruction of superconducting states in lanthanide metals. There are a considerable number of 4$f$ electrons in Gd, Tb, Dy, and other middle lanthanide metals, which leads to the ferromagnetism of them below the Curie temperature. By contrast, Yb and Lu metals have weak paramagnetism

---

[*] zhongxin@calypso.cn
[†] hyluphys@163.com
[‡] lucheng@calypso.cn

because of their fully filled $4f^{14}$ orbital configurations [18]. On the other hand, the La, Ce, and Po metals are nonmagnetic due to the small amount of $4f$ electrons. Among these lanthanides, the La, Ce, and Lu metals have been found to be superconductors under ambient pressure or high pressure with a $T_c$ of about 13 K [12,13]. Recently Song *et al.* [19] have reported that Yb is a superconductor with a $T_c$ of 1.4 K under 86 GPa and a $T_c$ of 4.6 K under 179 GPa. However, the detailed structures of Yb could not be derived from this experiment. In other words, they just declare that Yb becomes a superconductor for pressures above 86 GPa [19]. Therefore, it is prerequisite to determine the structural evolution and electronic properties of Yb under high pressure for further understanding the potential mechanism of superconductivity.

In the present work, we carry out systematical structural predictions of Yb under high pressure up to 240 GPa by the crystal structure analysis by particle swarm optimization (CALYPSO) method combined with first-principle calculations. Two phases, $R\bar{3}m$ and $I4/mmm$, of Yb are presented. Our calculations indicate that the structural phase transition sequence of Yb under high pressure is $R\bar{3}m \longrightarrow P3_121 \longrightarrow Im\bar{3}m \longrightarrow I4/mmm \longrightarrow P6_3/mmc$, which is different from the sequence of phase transitions for the regular trivalent lanthanide metals. Intriguingly, the $R\bar{3}m$-type Yb is a semimetal from ambient pressure to 1.8 GPa, and subsequently it transforms to the metallic states up to 240 GPa. The energy, lattice dynamics, and electronic properties show that the $P6_3/mmc$ phase of Yb is thermodynamically stable from 32 to 240 GPa, and it is found to be a good superconductor with the highest $T_c$ of 19.5 K at 160 GPa.

## II. COMPUTATIONAL METHODS

The ground state structures of Yb under high pressure are predicted by a crystal structure search method as implemented in the CALYPSO package [20,21]. The validity of the CALYPSO method in predicting the ground state structures has been confirmed by various experiments [22–25]. The structural relaxations, thermodynamic stabilities, and electronic and band structures are carried out by the Vienna *ab initio* simulation package (VASP) [26]. The Perdew-Burke-Ernzerhof (PBE) functionals and projector augmented wave potentials with $5s^25p^64f^{14}6s^2$ valence spaces are adopted to describe the exchange-correlation and electron-ion interactions [27,28]. The plane-wave basis set with a cutoff energy of 500 eV and dense $k$-point meshes with $2\pi \times 0.02$Å$^{-1}$ are used to ensure that the total energies of the searched structures are converged within 1 meV/atom.

The EPC calculations are performed by the QUANTUM ESPRESSO code based on the density functional perturbation theory [29]. Based on previous experiences and convergence tests [7,30], the ultrasoft pseudopotentials with $5s^25p^64d^{10}4f^{14}6s^2$ valence spaces are adopted to describe the electron-ion interactions. The kinetic cutoff energy is set to 140 Ry. The kind and value of smearing are Gaussian and 0.05, respectively. The Brillouin zone is sampled by $6 \times 6 \times 6$ $q$-point meshes and denser $24 \times 24 \times 24$ $k$-point meshes to calculate the EPC parameter ($\lambda$). The superconducting transition temperatures are obtained by solving the McMillan equation modified by Allen-Dynes [17] as follows:

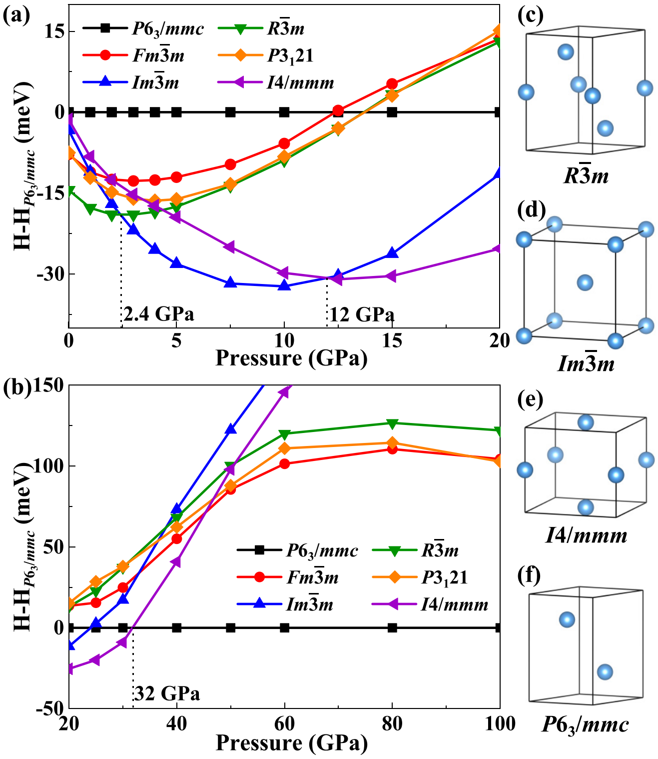

FIG. 1. Calculated enthalpies per atom of various phases of Yb under different pressures. (a) Enthalpy-pressure curves from ambient pressure to 20 GPa. (b) Enthalpy-pressure curves from 20 to 100 GPa. (c)–(f) Crystal structures of $R\bar{3}m$, $Im\bar{3}m$, $I4/mmm$, and $P6_3/mmc$ phases of Yb, respectively.

$$T_c = \frac{\omega_{log}}{1.2} \exp\left[\frac{-1.04(1+\lambda)}{\lambda(1-0.62\mu^*)-\mu^*}\right], \tag{1}$$

where $\omega_{log}$ is the logarithmic average of the phonon frequency, which can be expressed as

$$\omega_{log} = \exp\left[\frac{2}{\lambda}\int d\omega \frac{\alpha^2F(\omega)}{\omega}\log\omega\right]. \tag{2}$$

The accuracy of Eqs. (1) and (2) has been well verified by the superconductivity calculations of various systems [31].

## III. RESULTS AND DISCUSSION

We carry out variable-cell (from one to ten) and fixed-cell (two, four, six, eight, and ten) structural predictions for Yb under 0, 10, 30, 50, 100, 150, 200, and 250 GPa. We obtain about 1500 low-energy structures for each pressure. The experimentally observed phases, $Fm\bar{3}m$, $Im\bar{3}m$, $P6_3/mmc$, and $P3_121$, of Yb are successfully uncovered [32–35]. At the same time, several low-lying energy and highly symmetrical phases ($Immm$, $R\bar{3}m$, $I4/mmm$, $C2/m$, $Pm\bar{3}m$, and $Pnma$ structures, etc.) are also searched. The structural parameters are listed in Table S1 [36]. The enthalpy differences relative to the $P6_3/mmc$ structure under high pressure up to 240 GPa are shown in Figs. 1(a), 1(b), and S1(a) [36]. It can be seen from Fig. 1(a) that the $R\bar{3}m$ structure is more stable than the perviously observed $P6_3/mmc$ phase from ambient pressure to

2.4 GPa. Subsequently, the $R\bar{3}m$ phase transforms to the $Im\bar{3}m$ phase, which is consistent with the experimental data reported by Chesnut and Vohra [35]. Indeed, the low-temperature phase at ambient pressure is described as a hcp structure [32,33]. With increasing of the temperature, it may exhibit the phase transformation to a fcc phase and then to a bcc phase, which is because the energy discrepancies of these phases are small and just several meV/atom. Another phase of Yb is $I4/mmm$ symmetry, which is stable from 12 to 32 GPa [see Figs. 1(a) and 1(b)]. As pressure moderately increases, the $I4/mmm$ structure transitions to the $P6_3/mmc$ structure, which is stable up to 240 GPa. Actually, we have indeed found two other experimentally reported and energy closed phases of Yb, i.e., $Fm\bar{3}m$ and $P3_121$; however, they are about 40 meV/atom higher than the currently searched $P6_3/mmc$ structure. The crystal structures of Yb under high pressure are shown in Figs. 1(c)–(f) and Figs. S1(b) and S1(c) [36].

Considering the energy differences between different phases are less than 10 meV from ambient pressure to 5 GPa, we further introduce the zero-point energy (ZPE) into the calculations of the enthalpies of Yb from ambient pressure to 20 GPa. The energetic ranking of the structures of Yb are changed a little. The $P3_121$ phase is 0.4 meV/atom lower than the $R\bar{3}m$ phase at 2 GPa. The detailed results are shown in Fig. S2 [36]. It can be seen from Fig. S2 [36] that the $R\bar{3}m$ structure is still the most stable phase under ambient pressure. It subsequently transforms to the $P3_121$ phase at 1.8 GPa. As the pressure increases, the $P3_121$ phase transforms to the $Im\bar{3}m$ phase at 2.9 GPa. The ZPE has little effect on enthalpies of Yb when the pressure is higher than 5 GPa. One possible reason is that Yb is a heavy element with a relatively large atomic mass. The phase transition pressure from the $Im\bar{3}m$ phase to the $I4/mmm$ phase is 11.8 GPa, which is consistent with the above result of 12 GPa.

To explore the mechanical stabilities of Yb, we calculate the elastic constants by the strain stress method for $R\bar{3}m$, $Im\bar{3}m$, $I4/mmm$, and $P6_3/mmc$ phases under 0, 5, 20, and 50 GPa, respectively. The calculated elastic stiffness constants of these phases are listed in Table S2 [36] and satisfy the respective mechanical stability criteria. Notably, the value of $C_{33}$ for the $P6_3/mmc$ phase is smaller than the values of $C_{11}$ and $C_{22}$, revealing the $P6_3/mmc$ phase is easier to compress along the $c$ axis than along the $a$ and $b$ axes. On the contrary, the value of $C_{33}$ for the $P3_121$ phase is larger than the values of $C_{11}$ and $C_{22}$, indicating the $P3_121$ phase is harder to compress along the $c$ axis than along the $a$ and $b$ axes. The dynamical stabilities of the ground state and other low-energy structures are examined through the lattice dynamics calculations. The phonon dispersion curves of Yb under high pressure are shown in Fig. 2 and Fig. S3 [36], which reveal that all considered structures at corresponding pressure are stable with no imaginary frequency modes. Based on the calculated enthalpies and phonon dispersion curves as well as the mechanical stability analyses, we reasonably conclude that Yb metal shows the following sequence of phase transition with increasing pressure:

$$R\bar{3}m \xrightarrow{1.8} P3_121 \xrightarrow{2.9} Im\bar{3}m \xrightarrow{11.8} I4/mmm \xrightarrow{32} P6_3/mmc. \quad (3)$$

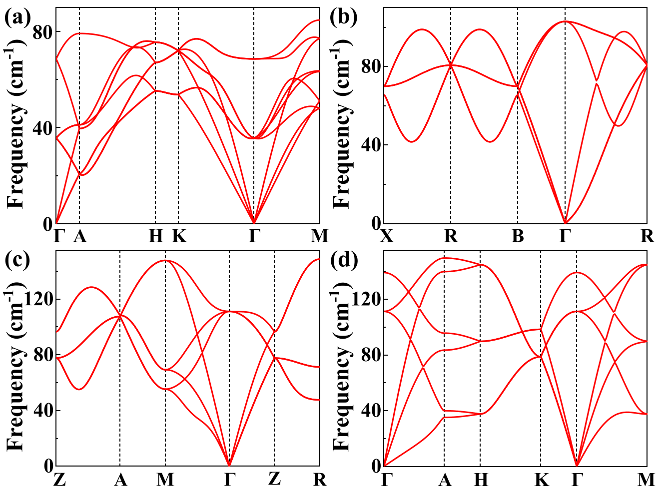

FIG. 2. Calculated phonon dispersion curves of Yb under different pressures. (a) $R\bar{3}m$ at ambient pressure, (b) $Im\bar{3}m$ at 5 GPa, (c) $I4/mmm$ at 20 GPa, and (d) $P6_3/mmc$ at 50 GPa.

However, a comparison of all available experiment results [32–35] and the above searched structural data, we find that this phase transition sequence is partially different from the traditional structural transformation sequence of regular lanthanides under high pressure [37]. This is, in part, due to the fact that the special electronic configuration of Yb, and sometimes the valence of Yb, is changed under high pressure [35,38]. In fact, we also consider the mechanical and dynamical stabilities of the experimentally reported phases (the $P6_3/mmc$ phase under 0 and 30 GPa, the $Fm\bar{3}m$ phase under 0 and 80 GPa, the $Im\bar{3}m$ phase under 20 GPa, and the $P3_121$ phase under 200 GPa, respectively). The calculated phonon dispersion curves are shown in Fig. S3 [36], which indicates the absence of any imaginary frequencies in the whole Brillouin zone. It can be seen from Figs. 1(a) and 1(b) that the energy differences between our phases and the experimentally observed phases are varied about 10 meV/atom at ambient pressure. Such small energy discrepancies could spontaneously cause the difficulty for distinguishing the ground state and the metastable state.

The previous high-pressure resistance measurements at room temperature show that Yb changes from semimetal to semiconductor under 1.4 GPa and is metallized at about 5 GPa [39]. The overt feature of semimetals in electronic band structures is that there exist slight overlaps between the valence band maximum (VBM) and the conduction band minimum (CBM), making the $N_{E_F}$ not zero at the Fermi level. Normally, pure elements with semimetal properties are concentrated on the transition lines between metals and nonmetals, such as As, Sb, Bi, etc. [40]. Recently, $TiS_2$ and $WSe_2$, formed by TMs and nonmetals, have also been discovered to be semimetal under high pressure [41,42]. To verify the true semimetal-semiconductor-metal transitions of Yb under high pressure, it is natural to put forward a question whether the $R\bar{3}m$ phase exhibits the homologous electronic properties? We subsequently calculate the electronic band structures and partial electronic density of states (PDOS) of the $R\bar{3}m$ phase under ambient pressure and 2 GPa (see Fig. 3). The electronic band

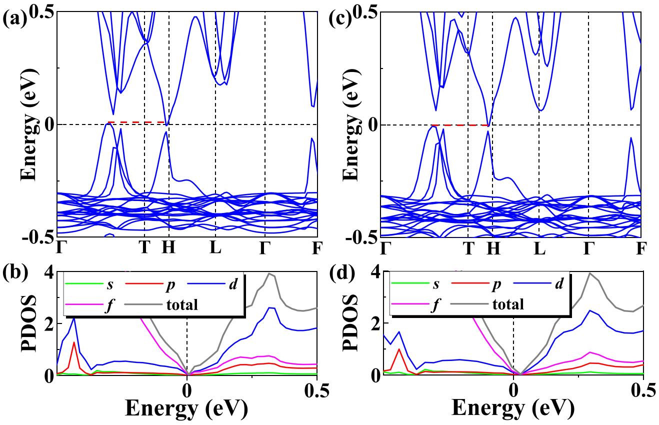

FIG. 3. (a) Calculated band structures of the $R\bar{3}m$ phase of Yb at ambient pressure. The red dashed line indicates that the VBM along the Γ-T high-symmetry path is slightly higher than the CBM at the H point. (b) Calculated PDOS of the $R\bar{3}m$ phase at ambient pressure. (c) Calculated band structures of the $R\bar{3}m$ phase at 2 GPa. The red dashed line indicates that the VBM along the Γ-T high-symmetry path is slightly higher than the CBM at the H point. (d) Calculated PDOS of the $R\bar{3}m$ phase at 2 GPa.

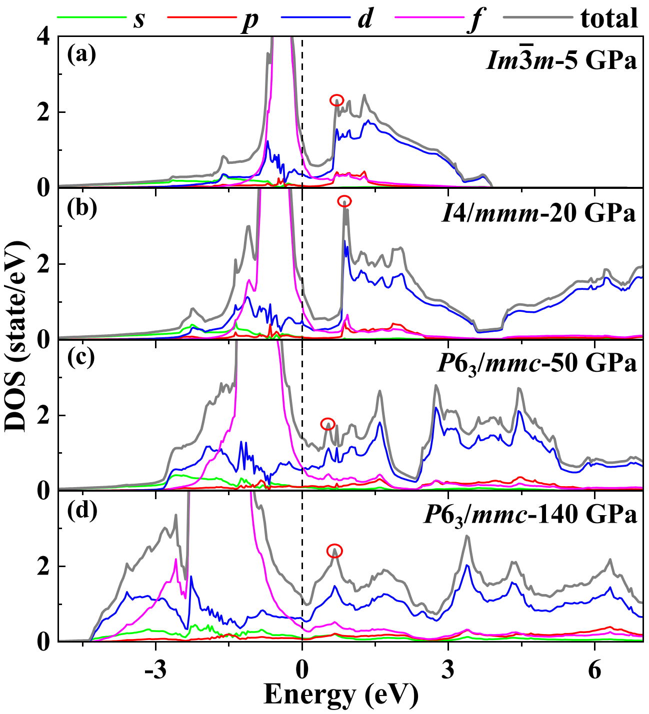

FIG. 4. Calculated partial-wave electron density of states of Yb under different pressures. (a) $Im\bar{3}m$ at 5 GPa, (b) $I4/mmm$ at 20 GPa, (c) $P6_3/mmc$ at 50 GPa, and (d) $P6_3/mmc$ at 140 GPa. The position indicated by the dashed line is the Fermi level, and the Van Hove singularities (red circles) appear in all phases.

structures of the $R\bar{3}m$ phase of Yb under ambient pressure, as shown in Fig. 3(a), reveal that the VBM along the Γ-T high-symmetry paths slightly overlaps with the CBM at the H point, which suggests that the $R\bar{3}m$ structure of Yb is likely to be a semimetal under ambient pressure. Moreover, the detailed PDOS indicates that the valence bands dominated by $d$ and $f$ orbitals occupy a part of the area above the Fermi level, making the $N_{E_F}$ slightly higher than zero [see Fig. 3(b)]. As the pressure increases to 2 GPa, the electronic band structures of the $R\bar{3}m$ phase of Yb are almost unchanged and show the semimetallic properties. Interestingly, the total electronic density of states (TDOS) of the $Im\bar{3}m$ phase at the Fermi level is about 1.25 state/eV under 5 GPa [as shown in Fig. 4(a)], which indicates that Yb not only undergoes the structural transition but also accompanies the semimetal to metal transition.

To investigate the electronic properties of Yb under high pressure, we calculate the PDOS of $Im\bar{3}m$ at 5 GPa, $I4/mmm$ at 20 GPa, and $P6_3/mmc$ at 50 and 140 GPa, respectively (see Fig. 4). The results show that Yb is always metallic at pressures above 5 GPa. On the whole, as pressure increases, the range of valence bands and conduction bands continually expands, which leads to the degree of overlaps between them near the Fermi level gradually increasing, thereby increasing the average electronic density of states near the Fermi level ($N_{nE_F}$). As shown in Fig 4(a), the $s$ orbitals hardly occupy the regions above the Fermi level at 5 GPa. Then the $s$ orbitals gradually move to the high-energy regions with pressure increases. When the pressure reaches up to 140 GPa, the contributions of $s$ orbitals to $N_{nE_F}$ can be compared with those of $p$ orbitals. Intriguingly, the trends of the DOS of $p$ orbitals are first different from those of $d$ orbitals, then gradually similar, and finally consistent with each other at 140 GPa.

It can be clearly seen from Fig. 4 that the 4$d$ orbitals occupy the dominant position, contribute more than 55% to the $N_{E_F}$, and cause the high-$T_c$ value of the $P6_3/mmc$ phase of Yb at 140 GPa. The 4$f$ orbitals contribute 58%, 46%, 44%, and 29% to the $N_{E_F}$ of Yb at 5, 20, 50, and 140 GPa, respectively. In addition, the contributions of 4$f$ orbitals to the $N_{E_F}$ decrease gradually as the pressure increases. Obviously, the $P6_3/mmc$ phase of Yb belongs to strong EPC interactions with a high number of 4$d$ states and a low number of 4$f$ states at the Fermi level under 140 GPa. Similar results are reported in $YbH_{10}$ [7]. The high numbers of H $s$ states and the low numbers of RE $f$ states at the Fermi level lead to the strong EPC interactions and the high-$T_c$ superconductivity of $YbH_{10}$ under high pressure. Recently, Chikina *et al.* [43] have achieved the transfer of the Van Hove singularity from a relatively far position to a position near the Fermi level by doping Pd into 2H-$TaSe_2$. The peak of the TDOS is fast shifted to the Fermi level, which leads to an order of magnitude increase of the superconducting transition temperature [44]. Interestingly, we also find the Van Hove singularities near the Fermi level, which are marked by the red circles in Fig. 4. The Van Hove singularity of Yb under 160 GPa is just below the Fermi level (see Fig. S6(f) [36]), and the corresponding value of $N_{E_F}$ is about 1.3 state/eV. The appearance of the Van Hove singularity near the Fermi level stimulates the electronic Cooper pairs and prompts the superconducting state of Yb.

To confirm the potential superconductivity of Yb, the phonon dispersion curves and EPC parameters are calculated under pressure from ambient pressure to 240 GPa. The superconducting critical temperature $T_c$ is obtained by solving the McMillan equation, i.e., Eq. (1). $T_c$ as a function of pressure

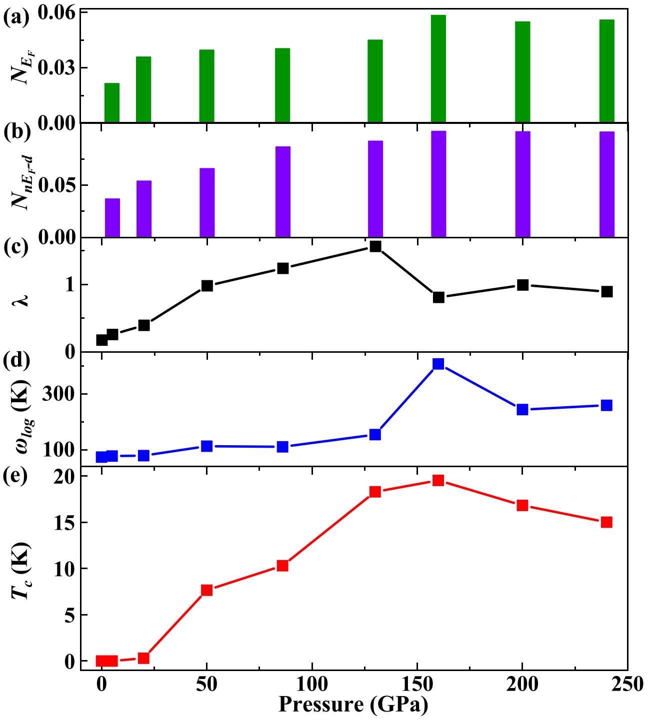

FIG. 5. Calculated $N_{E_F}$, $N_{nE_F-d}$, EPC parameter λ, $\omega_{log}$, and $T_c$ of Yb under different pressures. (a) $N_{E_F}$, (b) $N_{nE_F-d}$, (c) EPC parameter λ, (d) $\omega_{log}$, and (e) $T_c$. $N_{E_F}$ and $N_{nE_F-d}$ are the TDOS per unit volume and the average PDOS of $d$ orbitals per unit volume, respectively. The units are state/eV/Å$^3$.

is presented in Fig. 5(e). Generally, the superconductivity is positively correlated with the EPC parameter λ. Our results basically follow this rule, and the calculated EPC parameter λ increases monotonically with the pressure until 130 GPa; however, it decreases from 1.56 to 0.81 after the pressure exceeds 130 GPa. The $T_c$ value of the $P6_3/mmc$ phase of Yb at 130 GPa is 18.3 K with an EPC parameter λ of 1.56 and a Coulomb shielding constant $\mu^*$ of 0.1 [see Fig. 5(e)]. As for the $R\bar{3}m$ and $I4/mmm$ phases of Yb at low pressure, the band structures indicate the overlaps between the valence bands and the conduction bands in the energy range of −1.5 to 1.5 eV are limited under pressure below 30 GPa, resulting in the small $N_{E_F}$ and $N_{nE_F-d}$ [see Figs. 5(a) and 5(b)]. No appreciable $T_c$ values are observed for both the $Im\bar{3}m$ and $I4/mmm$ phases of Yb. With the pressure increase, the crystal structure of Yb transforms from the $I4/mmm$ phase to the $P6_3/mmc$ phase at 32 GPa, and the $T_c$ value of the metallic $P6_3/mmc$ phase under 50 GPa is 7.6 K. When the pressure increases to 130 GPa, the EPC parameter λ rapidly increases from 0.98 to the peak of 1.56 and the corresponding value of $T_c$ increases from 7.6 to 18.3 K. Although the stable pressure range of the metallic $P6_3/mmc$ phase of Yb is wide, ranging from 32 to 240 GPa, the superconductivity of $T_c$ begins to decrease slowly after pressures above 160 GPa. Encouragingly, the maximum $T_c$ value of 19.5 K for Yb under 160 GPa is visibly higher than the values for other lanthanides, such as La (6 K at ambient pressure, 13 K at 15 GPa), Ce (1.7 K at 5 GPa), Lu (12.4 K at 174 GPa) [12,13], etc. In fact, we have found that the experimentally reported $T_c$ of Yb at 100 GPa is about 1.5 K [19]. However, the measured sample is the $Fm\bar{3}m$ phase of Yb. We have calculated the $T_c$ of the $Fm\bar{3}m$ phase of Yb under 100 GPa. Our calculations show that the $T_c$ of Yb with $Fm\bar{3}m$ symmetry under 100 GPa is 1.6 K, which is in good agreement with the experimental value of 1.5 K [19]. Thus, the $P6_3/mmc$ phase of Yb currently has the highest $T_c$ for lanthanide superconductors, which needs to be further verified by future experiments.

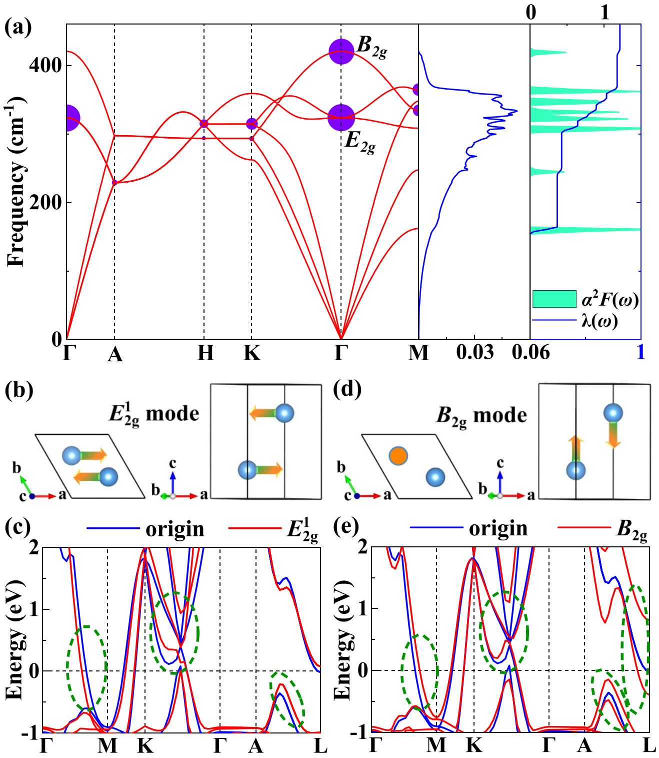

FIG. 6. (a) Calculated phonon dispersion curves, phonon density of states (PHDOS), Eliashberg function $\alpha^2F(\omega)$, and EPC parameter λ of the $P6_3/mmc$ phase of Yb under 160 GPa. The relative intensities of the EPC parameters $\lambda_{qv}$ are represented by the purple circles. (b) Vibration patterns of $E^1_{2g}$ phonon modes at the Γ point. (c) The influences of $E^1_{2g}$ phonon modes on the band structures. The greatest influences are circled by the green circles. (d) Vibration patterns of $B_{2g}$ phonon modes at the Γ point. The orange circle indicates the upward vibration direction. (e) The influences of $B_{2g}$ phonon modes on the band structures.

Figure 6(a) presents the phonon dispersion curves, the phonon density of states (PHDOS), the Eliashberg function $\alpha^2F(\omega)$, and the EPC parameter λ of the $P6_3/mmc$ phase of Yb under 160 GPa. The PHDOS and the EPC parameter λ reveal that the vibrations of Yb from 300 to 370 cm$^{-1}$ frequency modes contribute the most to the EPC parameter λ, which induces Yb to possess the highest $T_c$ (19.5 K) at 160 GPa with an EPC parameter λ of 0.81. The relative intensities of the EPC parameters $\lambda_{qv}$ at the high-symmetry points are represented by the purple circles in the phonon dispersion curves. It can be noticed that the $E_{2g}$ (degenerated by $E^1_{2g}$ and $E^2_{2g}$) and $B_{2g}$ phonon modes cause the strong EPC interactions at the Γ points.

To further explore the relations between the fully filled 4$d$ orbitals and the superconductivity of Yb, we consider the band structure changes before and after adding a perturbation to deform the lattice structure of Yb with an atomic displacement of 0.10 Å associated with the $E_{2g}^1$ and $B_{2g}$ phonon modes, respectively. The atomic vibrations of real-space diagrams corresponding to $E_{2g}^1$ and $B_{2g}$ phonon modes of the $P6_3/mmc$ phase of Yb under 160 GPa are shown in Figs. 6(b) and 6(d), which plainly display that the $E_{2g}^1$ and $B_{2g}$ modes correspond to the relative vibrations of Yb atoms along the $a$ and $c$ directions, respectively. The band structure changes caused by the two modes are marked by green circles in Figs. 6(c) and 6(e). Because the orbitals are closely related, we calculate the orbit-resolved band structures, as shown in Fig. 7, to determine the changes of two modes on band structures and distinguish the correlated orbitals. The rest of the orbit-resolved band structures with weak correlation orbitals are shown in Figs. S6(a)–S6(e) [36]. It can be clearly seen from Figs. 6(c) and 7 and Figs. S6(a)–S6(e) [36] that the $E_{2g}^1$ modes mainly change the band structures corresponding to the $d_{x^2-y^2}$, $d_{xz}$, and $d_{yz}$ orbitals and weakly affect the band structures corresponding to the $s$ orbital. The band structures corresponding to the rest of the orbitals are almost unaffected by the $E_{2g}^1$ modes. This indicates that the $\pi$-bonding electrons formed by the $d_{x^2-y^2}$, $d_{xz}$, and $d_{yz}$ orbitals strongly couple with the $E_{2g}^1$ phonon modes near the Fermi level. The main influences of the $B_{2g}$ modes on the band structures are marked by the green circles in Fig. 6(e). By contrast, the $B_{2g}$ modes primarily affect the band structures corresponding to the $d_{z^2}$ orbitals and weakly affect the band structures corresponding to the $d_{xy}$, $d_{xz}$, $d_{yz}$, and $s$ orbitals, which indicates that there is a strong coupling between the $\sigma$-banding electrons formed by the $d_{z^2}$ orbitals and the $B_{2g}$ phonon modes in Yb under high pressure. In fact, the $E_{2g}^1$ and $B_{2g}$ phonon modes are related to the EPC interactions. Thus, the $d_{x^2-y^2}$, $d_{z^2}$, $d_{xy}$, $d_{xz}$, and $d_{yz}$ orbitals are, in principle, contributing to the superconductivity of Yb under high pressure. Furthermore, the changes of $N_{nE_F-d}$ and the EPC parameter $\lambda$ show that the higher $N_{nE_F-d}$ values correspond to the stronger EPC interactions at pressures from ambient pressure to 130 GPa [see Figs. 5(b) and 5(c)]. But, the EPC parameter $\lambda$ decreases at pressures above 130 GPa with relatively high $N_{nE_F-d}$. To find the underlying reason for this abnormal behavior, we calculate the electronic local functions (ELFs) of Yb at 86 and 160 GPa, as shown in Fig. S5 [36]. It can be seen from Fig. S5(a) [36] that a strong discrete region between the nearest-neighbor Yb atoms is found at 86 GPa, which is not conducive to the conduction of free electrons. Through further analysis, we found that the distance of nearest-neighbor Yb atoms is 2.80 Å, which is much smaller than the Yb-Yb covalent bond of 3.74 Å [45], leading to a lot of overlaps of the outer electron clouds for the nearest-neighbor Yb atoms. The distance of the second-nearest-neighbor Yb atoms is about 4.30 Å, and naturally a certain free electron region is observed between the second-nearest-neighbor atoms. Meanwhile, the metallic bonds are formed between the third-nearest-neighbor Yb atoms, which play a dominant role in the conduction of electrons. When the pressure increases to 160 GPa, external compression squeezes the crystal lattices and compels the distances between nearest-neighbor, second-nearest-neighbor, and third-nearest-neighbor Yb atoms to further reduce, which makes it difficult for nearest-neighbor Yb atoms to conduct electrons as before, the free electronic areas between the second-nearest-neighbor Yb atoms disappear, and the metal bonds between the third-nearest-neighbor Yb atoms become weaker (see Fig. S5(b) [36]). Thus, although considerable $N_{E_F}$ and $N_{nE_F-d}$ values are possessed at pressures above 130 GPa, the EPC interactions decrease due to the lack of abundant paths for conducting the active electrons. Overall, the increase of the electronic density of states for $d$ orbitals near the

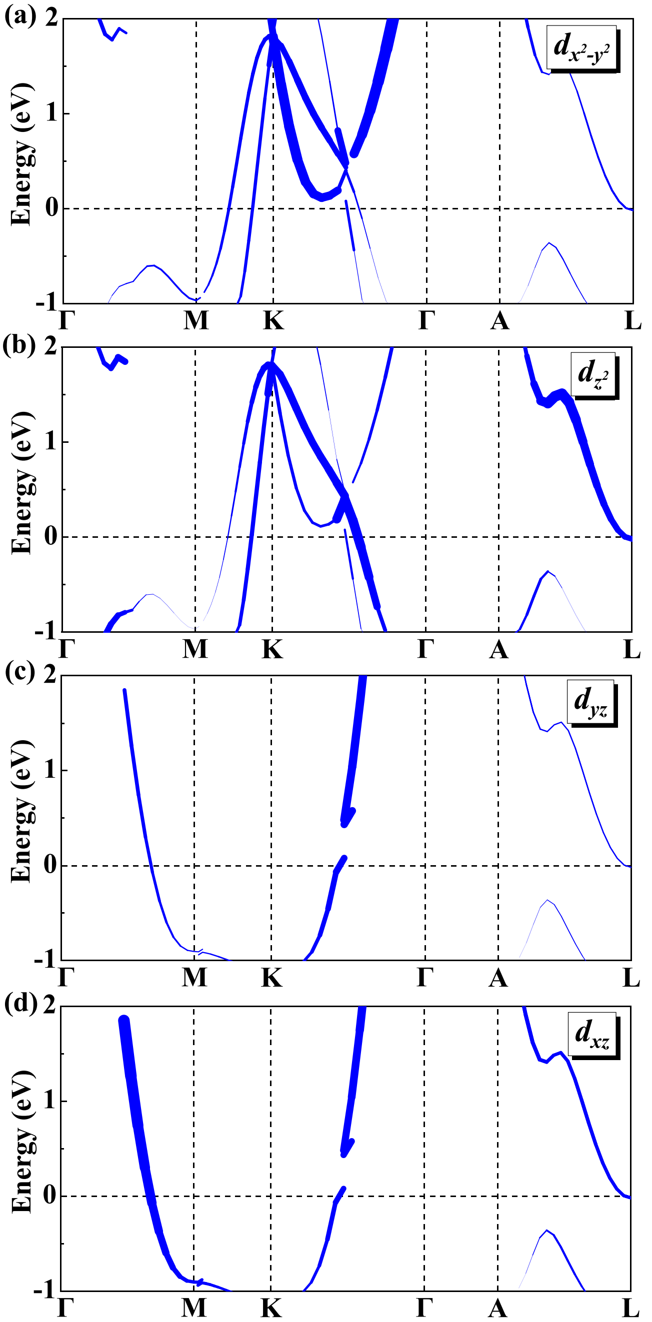

FIG. 7. Calculated orbital-resolved band structures corresponding to different orbitals of the $P6_3/mmc$ phase of Yb under 160 GPa. (a) $d_{x^2-y^2}$, (b) $d_{z^2}$, (c) $d_{yz}$, and (d) $d_{xz}$ orbitals. The thicknesses of curves represent the weight of orbitals in the corresponding band structures.

Fermi level is expected to enhance the EPC interactions and the superconducting transition temperature of Yb under high pressure.

## IV. CONCLUSION

In summary, we carry out a theoretical study on the structural phase transition and superconductivity of Yb under high pressure by crystal structure prediction and first-principle calculations. Two alternative structures of Yb with $R\bar{3}m$ and $I4/mmm$ symmetries are presented. The $R\bar{3}m$ structure possesses the semimetallic properties from ambient pressure to 2 GPa, and the $I4/mmm$ structure is a metallic phase stabilized from 11.8 to 32 GPa. Most importantly, the $P6_3/mmc$ phase of Yb is found to be an outstanding superconductor with a $T_c$ value of 19.5 K at 160 GPa, which is the highest $T_c$ for lanthanide superconductors. The high $T_c$ of Yb under high pressure is attributed to the abundant $4d$ states and low $4f$ states at the Fermi level. These findings establish a different structural phase transition sequence of Yb under high pressure, which offers crucial insights for design of the more complex lanthanide-based superconductor.

## ACKNOWLEDGMENTS

This work is supported by the National Natural Science Foundation of China under Grants No. 12111530103 and No. 12174352 and by the CAEP Project under Grant No. TCGH0710.

[1] N. W. Ashcroft, Phys. Rev. Lett. **21**, 1748 (1968).

[2] N. W. Ashcroft, Phys. Rev. Lett. **92**, 187002 (2004).

[3] Y. Li, J. Hao, H. Liu, Y. Li, and Y. Ma, J. Chem. Phys. **140**, 174712 (2014).

[4] D. Duan, Y. Liu, F. Tian, D. Li, X. Huang, Z. Zhao, H. Yu, B. Liu, W. Tian, and T. Cui, Sci. Rep. **4**, 6968 (2014).

[5] A. P. Drozdov, M. I. Eremets, I. A. Troyan, V. Ksenofontov, and S. I. Shylin, Nature (London) **525**, 73 (2015).

[6] H. Liu, I. I. Naumov, R. Hoffmann, N. W. Ashcroft, and R. J. Hemley, Proc. Natl. Acad. Sci. USA **114**, 6990 (2017).

[7] W. Sun, X. Kuang, H. D. J. Keen, C. Lu, and A. Hermann, Phys. Rev. B **102**, 144524 (2020).

[8] W. Chen, D. V. Semenok, X. Huang, H. Shu, X. Li, D. Duan, T. Cui, and A. R. Oganov, Phys. Rev. Lett. **127**, 117001 (2021).

[9] G. Gao, L. Wang, M. Li, J. Zhang, R. T. Howie, E. Gregoryanz, V. V. Struzhkin, L. Wang, and J. S. Tse, Mater. Today Phys. **21**, 100546 (2021).

[10] H. Xie, Y. Yao, X. Feng, D. Duan, H. Song, Z. Zhang, S. Jiang, S. A. T. Redfern, V. Z. Kresin, C. J. Pickard, and T. Cui, Phys. Rev. Lett. **125**, 217001 (2020).

[11] A. P. Drozdov, P. P. Kong, V. S. Minkov, S. P. Besedin, M. A. Kuzovnikov, S. Mozaffari, L. Balicas, F. F. Balakirev, D. E. Graf, V. B. Prakapenka *et al.*, Nature (London) **569**, 528 (2019).

[12] M. Debessai, J. J. Hamlin, and J. S. Schilling, Phys. Rev. B **78**, 064519 (2008).

[13] J. A. Flores-Livas, L. Boeri, A. Sanna, G. Profeta, R. Arita, and M. Eremets, Phys. Rep. **856**, 1 (2020).

[14] H. M. Tütüncü and G. P. Srivastava, J. Appl. Phys. **112**, 093914 (2012).

[15] J. Bardeen, L. N. Cooper, and J. R. Schrieffer, Phys. Rev. **108**, 1175 (1957).

[16] W. L. McMillan, Phys. Rev. **167**, 331 (1968).

[17] P. B. Allen and R. C. Dynes, Phys. Rev. B **12**, 905 (1975).

[18] J. M. Lock, Proc. Phys. Soc., Sect. B **70**, 476 (1957).

[19] J. Song, G. Fabbris, W. Bi, D. Haskel, and J. S. Schilling, Phys. Rev. Lett. **121**, 037004 (2018).

[20] Y. Wang, J. Lv, L. Zhu, and Y. Ma, Phys. Rev. B **82**, 094116 (2010).

[21] Y. Wang, J. Lv, L. Zhu, and Y. Ma, Comput. Phys. Commun. **183**, 2063 (2012).

[22] X. Liang, A. Bergara, L. Wang, B. Wen, Z. Zhao, X. F. Zhou, J. He, G. Gao, and Y. Tian, Phys. Rev. B **99**, 100505(R) (2019).

[23] X. Dou, X. Kuang, W. Sun, G. Jiang, C. Lu, and A. Hermann, Phys. Rev. B **104**, 224510 (2021).

[24] X. Liang, A. Bergara, X. Wei, X. Song, L. Wang, R. Sun, H. Liu, R. J. Hemley, L. Wang, G. Gao, and Y. Tian, Phys. Rev. B **104**, 134501 (2021).

[25] B. Chen, L. J. Conway, W. Sun, X. Kuang, C. Lu, and A. Hermann, Phys. Rev. B **103**, 035131 (2021).

[26] G. Kresse and D. Joubert, Phys. Rev. B **59**, 1758 (1999).

[27] G. Kresse and J. Furthmüller, Phys. Rev. B **54**, 11169 (1996).

[28] J. P. Perdew, K. Burke, and M. Ernzerhof, Phys. Rev. Lett. **77**, 3865 (1996).

[29] P. Giannozzi, S. Baroni, N. Bonini, M. Calandra, R. Car, C. Cavazzoni, D. Ceresoli, G. L. Chiarotti, M. Cococcioni, I. Dabo *et al.*, J. Phys.: Condens. Matter **21**, 395502 (2009).

[30] H. Song, Z. Zhang, T. Cui, C. J. Pickard, V. Z. Kresin, and D. Duan, Chin. Phys. Lett. **38**, 107401 (2021).

[31] M. Gao, X. Kong, Z. Lu, and T. Xiang, Acta Phys. Sin. **64**, 214701 (2015).

[32] E. Bucher, P. H. Schmidt, A. Jayaraman, K. Andres, J. P. Maita, K. Nassau, and P. D. Dernier, Phys. Rev. B **2**, 3911 (1970).

[33] F. X. Kayser, Phys. Rev. Lett. **25**, 662 (1970).

[34] Y. C. Zhao, F. Porsch, and W. B. Holzapfel, Phys. Rev. B **49**, 815 (1994).

[35] G. N. Chesnut and Y. K. Vohra, Phys. Rev. Lett. **82**, 1712 (1999).

[36] See Supplemental Material at http://link.aps.org/supplemental/10.1103/PhysRevB.105.214503 for details of the structural and electronic properties of ytterbium under high pressure.

[37] U. Benedict, W. A. Grosshans, and W. B. Holzapfel, Physica B+C (Amsterdam) **144**, 14 (1986).

[38] K. Syassen, G. Wortmann, J. Feldhaus, K. H. Frank, and G. Kaindl, Phys. Rev. B **26**, 4745 (1982).

[39] A. B. Garg, V. Vijayakumar, and B. K. Godwal, Rev. Sci. Instrum. **75**, 2475 (2004).

[40] G. A. Saunders, Contemp. Phys. **14**, 149 (1973).

[41] D. R. Allan, A. A. Kelsey, S. J. Clark, R. J. Angel, and G. J. Ackland, Phys. Rev. B **57**, 5106 (1998).

[42] B. Liu, Y. Han, C. Gao, Y. Ma, G. Peng, B. Wu, C. Liu, Y. Wang, T. Hu, X. Cui *et al.*, J. Phys. Chem. C **114**, 14251 (2010).

[43] A. Chikina, A. Fedorov, D. Bhoi, V. Voroshnin, E. Haubold, Y. Kushnirenko, K. H. Kim, and S. Borisenko, npj Quantum Mater. **5**, 22 (2020).

[44] V. Sunko, E. A. Morales, I. Marković, M. E. Barber, D. Milosavljević, F. Mazzola, D. A. Sokolov, N. Kikugawa, C. Cacho, P. Dudin *et al.*, npj Quantum Mater. **4**, 46 (2019).

[45] B. Cordero, V. Gómez, A. E. Platero-Prats, M. Revés, J. Echeverría, E. Cremades, F. Barragán, and S. Alvarez, Dalton Trans. **21**, 2832 (2008).